

The Spin of the Supermassive Black Hole in NGC 3783

L. W. Brenneman¹, C. S. Reynolds^{2,3}, M. A. Nowak⁴, R. C. Reis⁵, M. Trippe²,
A. C. Fabian⁵, K. Iwasawa⁶, J. C. Lee⁷, J. M. Miller⁸, R. F. Mushotzky^{2,3}, K. Nandra⁹,
M. Volonteri⁸

ABSTRACT

The *Suzaku* AGN Spin Survey is designed to determine the supermassive black hole spin in six nearby active galactic nuclei (AGN) via deep *Suzaku* stares, thereby giving us our first glimpse of the local black hole spin distribution. Here, we present an analysis of the first target to be studied under the auspices of this Key Project, the Seyfert galaxy NGC 3783. Despite complexity in the spectrum arising from a multi-component warm absorber, we detect and study relativistic reflection from the inner accretion disk. Assuming that the X-ray reflection is from the surface of a flat disk around a Kerr black hole, and that no X-ray reflection occurs within the general relativistic radius of marginal stability, we determine a lower limit on the black hole spin of $a \geq 0.88$ (99% confidence). We examine the robustness of this result to the assumption of the analysis, and present a brief discussion of spin-related selection biases that might affect flux-limited samples of AGN.

¹Harvard-Smithsonian CfA, 60 Garden St. MS-67, Cambridge, MA 02138 USA

²Dept. of Astronomy, University of Maryland, College Park, MD 20742 USA

³Joint Space Science Institute (JSI), University of Maryland, College Park, MD 20742 USA

⁴MIT Kavli Institute for Astrophysics, Cambridge, MA 02139 USA

⁵Institute of Astronomy, University of Cambridge, Madingley Rd., Cambridge CB3 0HA, UK

⁶Universitat de Barcelona

⁷Dept. of Astronomy, Harvard University, Harvard-Smithsonian CfA, 60 Garden St. MS-6, Cambridge, MA 02138 USA

⁸Dept. of Astronomy, University of Michigan, Ann Arbor, Michigan 48109 USA

⁹Max-Planck-Institut für Extraterrestrische Physik, Giessenbachstrasse 1, 85740 Garching, Germany

1. Introduction

Ever since the seminal work of Penrose (1969) and Blandford & Znajek (1977), it has been recognized that black hole spin may be an important source of energy in astrophysics. Of particular note is the role that black hole spin may play in relativistic jets such as those seen in radio-loud active galactic nuclei (AGN) — the magnetic extraction of the rotational energy of a rapidly spinning black hole is the leading contender for the fundamental energy source of such jets. Indeed, it has been suggested that the spin of the central supermassive black hole (SMBH) is a crucial parameter in determining whether an AGN can form powerful jets (i.e., whether the source is radio-quiet or radio-loud; Wilson & Colbert 1995), although the accretion rate/mode must clearly have a role to play (Sikora et al. 2007).

However, the importance of black hole spin goes beyond its role as a possible power source. The spin distribution of the SMBH population (and its dependence on SMBH mass) encodes the black hole growth history (Moderski & Sikora 1996; Volonteri et al. 2005; Berti & Volonteri 2008). In essence, if local SMBHs have obtained most of their mass during prolonged prograde accretion events in a quasar phase of activity, or in major mergers with similar mass SMBHs, we would expect a population of rapidly rotating SMBHs ($a > 0.6$) due to the angular momentum accreted from the disks or transferred at merger (Rezzolla et al. 2008). Here we define $a \equiv cJ/GM^2$, where J is the angular momentum of the black hole and M is its mass. On the other hand, if mergers with much smaller SMBHs (Hughes & Blandford 2003) or randomly-oriented accretion events of small packets of material (King & Pringle 2007) have been the dominant growth mechanism, most of the SMBHs would be spinning at a much more modest rate.

To date, the cleanest probe of strong gravitational physics around SMBHs, including the effects of black hole spin, comes from examining relativistically-broadened spectral features that are emitted from the surface layers of the inner accretion disk in response to irradiation by the hard X-ray source (Reynolds & Nowak 2003; Miller 2007). These spectral features have been observed and well-characterized in both AGN (Tanaka et al. 1995; Fabian et al. 1995) and stellar-mass black hole systems (Miller et al. 2002; Reis et al. 2008). The strongest feature in this so-called “reflection spectrum” is the fluorescent Fe K α line (rest frame energy of 6.4 keV); in contrast to lines from other elements, its relative abundance, high energy and fluorescent yield make Fe K α visible above the typical power-law continuum seen commonly in BH systems. Extreme Doppler effects and gravitational redshifts combine to give this line (and all other features in the reflection spectrum) a characteristic broadened and skewed profile (Fabian et al. 1989; Laor 1991). Modern high signal-to-noise (S/N) datasets from *XMM-Newton* and *Suzaku*, combined with the latest models of reflection from an ionized accretion disk (e.g., Ross & Fabian 2005) and variable-spin relativistic smearing models (e.g.,

Brenneman & Reynolds 2006; Dauser et al. 2010), are giving us our first glimpses at the spins of SMBHs. However, due to the high S/N required to characterize the subtle effects of SMBH spin, interesting spin constraints have only been determined for a small handful of AGN at present (MCG–6-30-15, Brenneman & Reynolds 2006; Fairall 9, Schmoll et al. 2009; SWIFT J2127.4+5654, Miniutti et al. 2009; 1H0707–495, Zoghbi et al. 2010; Mrk 79, Gallo et al. 2011; Mrk 335 & NGC 7469 Patrick et al. 2010; see Table 2).

Under the auspices of the *Suzaku* Key Projects program, we have initiated a series of deep quasi-continuous observations of bright, nearby AGN with the purpose of characterizing relativistic disk features in the spectra and setting constraints on the SMBH spin (*Suzaku* AGN Spin Survey; *PI C. Reynolds*). In this *Paper*, we present results from the first object to be studied under this program, the Seyfert 1.5 galaxy NGC 3783 ($z = 0.00973$; Theureau et al. 1998). This object possesses a high-column density and multi-component warm absorber that has been well-studied by every spectroscopic X-ray observatory, including a 900 ks campaign by *Chandra* using the High-Energy Transmission Grating Spectrometer (HETGS; Kaspi et al. 2002; Krongold et al. 2003; Netzer et al. 2003). We show that, despite the presence of this complex warm absorber, reflection signatures from the inner accretion disk can be identified and characterized with sufficient accuracy to constrain SMBH spin. We conclude that the SMBH is rapidly spinning with $a > 0.93$ (90% confidence). This result is shown to be robust to the exclusion of the complex, soft region of the X-ray spectrum as well as to uncertainties in the XIS/PIN cross-normalization.

This paper is organized as follows. Section 2 discusses the *Suzaku* observation of NGC 3783 and the basic reduction of the data. Section 3 then presents our modeling of the 0.7 – 45 keV time-averaged spectrum of NGC 3783, including our newly-derived constraints on the SMBH spin. Section 4 summarizes our conclusions on NGC 3783 and addresses the role of spin-dependent selection biases in AGN samples.

2. Observations and Data Reduction

NGC 3783 was observed by *Suzaku* quasi-continuously for the period 10–15 July 2009, with the source placed in the Hard X-ray Detector (HXD) nominal aimpoint. After eliminating Earth occultations, South Atlantic Anomaly (SAA) passages, and other high background periods, the observation contains 210 ks of “good” on-source exposure. The XIS data (XIS 0, XIS 1 and XIS 3; XIS 2 has been inoperable since November 2006) were reprocessed using the `xispi` script in accordance with the *Suzaku* ABC Guide¹ along with the latest version of the

¹<http://heasarc.gsfc.nasa.gov/docs/suzaku/analysis/abc/>

CALDB (as of 29 March, 2010). XIS spectra and light curves were then produced according to the procedure outlined in the ABC Guide. For the XIS spectra, we combined data from the front-illuminated (FI) detectors XIS 0+3 data using the `addascaspec` script in order to increase S/N. The XIS spectra, responses and backgrounds were then rebinned to 512 spectral channels from the original 4096 in order to speed up spectral model fitting without compromising the resolution of the detectors. Finally, the XIS spectra were grouped to a minimum of 25 counts per bin in order to facilitate robust χ^2 fitting. The merged, background-subtracted, time-averaged FI spectrum has a net count rate of $4.960 \pm 0.002 \text{ cts s}^{-1}$ for a total of 1.04×10^6 counts. The total number of 2 – 10 keV counts is 6.26×10^5 . The total XIS 1 count rate is $3.043 \pm 0.004 \text{ cts s}^{-1}$ for a total of 6.40×10^5 , or 3.14×10^5 when restricting to 2 – 10 keV. For all of the fitting presented in this paper, we allow for a global flux cross-normalization error between the FI and XIS 1 spectra. The XIS 1/FI cross-normalization is allowed to be a free parameter, and is found to be approximately 1.03.

The HXD/PIN instrument detected NGC 3783, though the GSO did not. Data from PIN were again reduced as per the *Suzaku* ABC Guide. For background subtraction, we used the “tuned” non X-ray background (NXB) event file for July 2009 from the *Suzaku* CALDB, along with the appropriate response file and flat field file for epoch 5 data. The NXB background contributed a count rate of $0.2165 \pm 0.0004 \text{ cts s}^{-1}$ to the total X-ray background from 16 – 45 keV. We modeled the cosmic X-ray background (CXB) contribution as per the ABC Guide, simulating its spectrum in XSPEC (Arnaud 1996). The simulated CXB spectrum contributed a count rate of $0.0237 \pm 0.0002 \text{ cts s}^{-1}$ to the total X-ray background from 16 – 45 keV. The NXB and CXB files were combined to form a single PIN background spectrum. In comparison, the PIN data had a count rate of $0.4561 \pm 0.0027 \text{ cts s}^{-1}$ over the same energy range, roughly twice that of the total background.

Because the PIN data only contain 256 spectral channels (vs. the 4096 channels in the unbinned XIS data), rebinning to 25 counts per bin was not necessary in order to facilitate χ^2 fitting. Rather, we rebinned the PIN spectrum to have a S/N of 5 in each energy bin, which limited our energy range to 16 – 45 keV. After reduction, filtering and background subtraction, the PIN spectrum had a net 16 – 45 keV count rate of $0.360 \pm 0.002 \text{ cts s}^{-1}$. We also added 3% systematic errors to the PIN data to account for the uncertainty in the non-X-ray background data supplied by the *Suzaku* calibration team. For most of the spectral fitting presented in this paper, we assume a PIN/XIS-FI cross-normalization factor of 1.18 as per the *Suzaku* memo 2008-06². However, for the final fits used to constrain the black hole spin in §3.4, we investigate the effect of allowing this cross-normalization to be a free

²<http://heasarc.gsfc.nasa.gov/docs/suzaku/analysis/watchout.html>

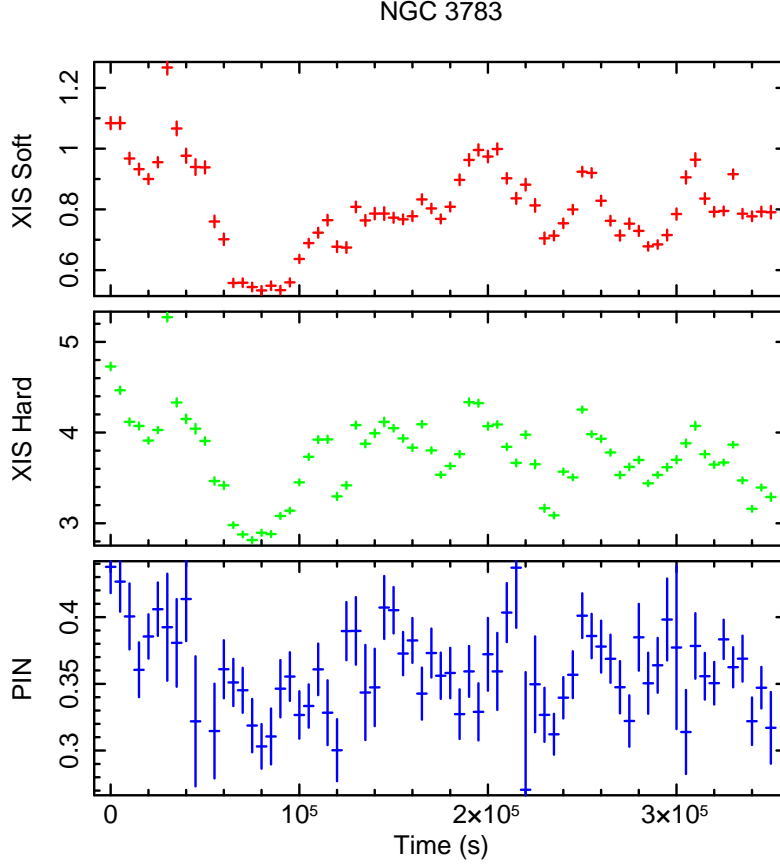


Fig. 1.— Co-added and background subtracted XIS light curves in the soft (0.3 – 1 keV) and hard (2 – 10 keV) bands, together with the background subtracted PIN (16 – 45 keV) light curve. These light curves are shown with 5000 s bins.

parameter.

XIS light curves (both hard and soft band) as well as PIN light curves are shown in Fig. 1. In the soft band (0.3 – 1 keV), the source is observed to undergo variability by a factor of almost two. Most of the large amplitude variability occurs on timescales of 50 – 100 ks, although there are occasional sharp flares/dips that occur much more rapidly. Also noteworthy is that the amplitude of variability decreases as one considers higher-energy bands, suggesting “pivoting” of the spectrum about some energy above the *Suzaku*/PIN band. The detailed nature of this spectral variability will be the subject of another publication (Reis et al., in preparation). For the remainder of this paper, we examine the high S/N spectrum from the time-averaged dataset. We restrict our energy range to 0.7 – 10 keV in the XIS data, ignoring energies below 0.7 keV and from 1.5 – 2.5 keV to avoid areas of significant

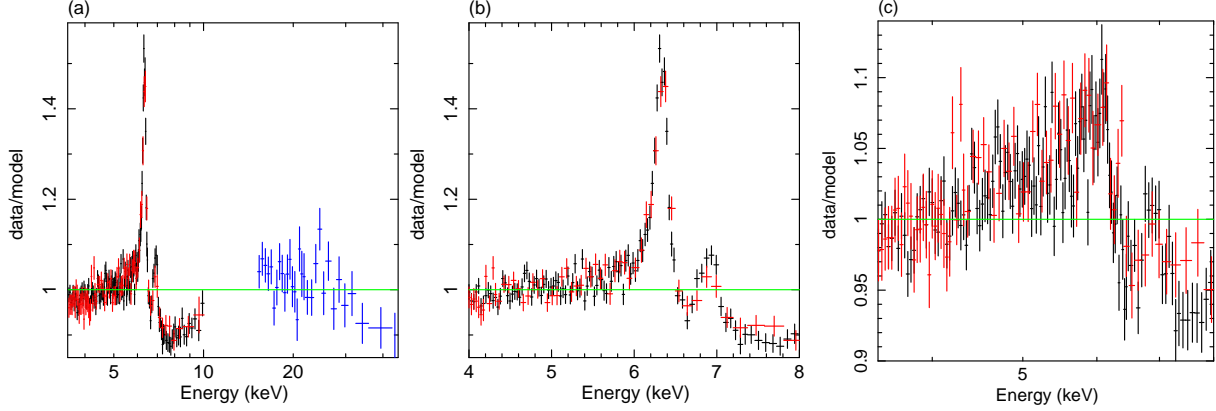


Fig. 2.— *Left panel:* Simple power-law fit to the 3.5–45 keV XIS-FI+PIN spectrum. *Middle panel:* Zoom-in on the 4–8 keV region of the simple power-law fit. Note the probable “Compton shoulder” on the immediate low-energy side of the strong 6.4 keV emission line. *Right panel:* Residuals remaining when the broad iron line component is removed from a simple phenomenological fit to the 3.5 – 45 keV data (see §3.1). In all panels the black points correspond to XIS 0+3 data, red to XIS 1 data and blue to PIN data. The green line represents a data-to-model ratio of unity.

deviation between the three detectors, i.e., regions of known calibration uncertainty.

3. Analysis of the time-averaged *Suzaku* spectrum

3.1. A First Look at the Hard-band Spectrum

It is instructive to begin by examining the hard-band (3.5–45 keV) XIS+PIN spectrum. A simple power-law fit to this band reveals significant spectral complexity (Fig. 2a,b). A narrow $K\alpha$ fluorescence line of cold iron (6.4 keV) dominates; structure redward of this line indicates a possible Compton shoulder as well as an extended tail reaching down to ~ 4 keV. Both the narrow iron line and the broad red wing likely originate from X-ray reflection and, hence, the convex spectrum between 8 – 40 keV is readily interpreted as the associated Compton reflection hump. Structure above the 6.4 keV line indicates a strong absorption feature at ~ 6.6 keV and/or an emission line at ~ 7 keV (likely corresponding to a blend of the $K\beta$ line of cold iron and the $Ly\alpha$ line of Fe XXVI).

Guided by these identifications, we construct an heuristic model of the hard spectrum consisting of a power-law continuum, a narrow Fe XXVI emission line (modeled as a Gaussian line centered at 6.97 keV with $\sigma = 10$ eV), reflection from distant, low-velocity, cold

matter (described by the **pexmon** model³), and a relativistically broadened cold iron $K\alpha$ line (described by the **laor** model; Laor 1991). This model produces an excellent fit to the data ($\chi^2/\nu = 573/544$ (1.05)) with the following parameters: photon index $\Gamma = 1.68^{+0.01}_{-0.01}$, reflection fraction $\mathcal{R} = 0.87^{+0.02}_{-0.06}$, emission line equivalent widths $W_{\text{FeXXVI}} = 28^{+4}_{-5}$ eV, $W_{\text{broad}} = 263^{+23}_{-23}$ eV, inner edge of line emitting disk $r_{\text{in}} = 3.0^{+0.1}_{-0.8} r_g$, index of line emissivity across disk $q = 3.31^{+0.06}_{-0.09}$, and disk inclination $i < 9^\circ$. If we replace the **pexmon** model with a **pexrav** and three separate Gaussian lines for narrow Fe $K\alpha$ (6.4 keV, $\sigma = 0.015$ keV), Fe $K\beta$ (7.06 keV, $\sigma = 0.015$ keV) and Compton shoulder (6.25 keV, $\sigma = 0.1$ keV), their equivalent widths are $W_{K\alpha} = 98^{+5}_{-5}$ eV, $W_{K\beta} \leq 8$ eV, and $W_{\text{CS}} = 22^{+8}_{-6}$ eV, respectively. We note that, in this fit, the intrinsic widths of the iron lines were taken from their *Chandra*/HETG values (Yaqoob et al. 2005). Substituting the individual Gaussian lines and **pexrav** component for the **pexmon** model results in a modest change in the global goodness-of-fit ($\Delta\chi^2/\Delta\nu = -32/-3$), likely owing to the free normalizations of the emission lines (they are set at fixed ratios within **pexmon**). No statistically significant change is seen in the other model parameters.

For illustrative purposes only, Fig. 2c shows the residuals that remain when the broad iron line is removed from this spectral model, and the remaining model parameters are re-fit. An obvious broad line remains. However, there are two reasons why this cannot be interpreted as the “the broad line profile” for this object. Firstly, NGC 3783 has a well-known, high-column density warm absorber that, while principally affecting the soft spectrum, can also introduce subtle spectral curvature up to 10 keV or more. Secondly, the broadened iron line is just the tip of the iceberg; especially when the accretion disk is ionized, the rest of the reflection spectrum has a sub-dominant but significant contribution that must be considered. The statistically unlikely value of the disk inclination derived from the simple fit ($i < 9^\circ$) is a signal of these issues. For these reasons, we are forced into global modeling of the full 0.7 – 45 keV spectrum.

³The **pexmon** model (Nandra et al. 2007) is a modification of the commonly used *pexrav* model (Magdziarz & Zdziarski 1995) which, in addition to the Compton backscattered reflection continuum, also models the $K\alpha$ and $K\beta$ emission lines of iron, the Compton shoulder of the iron $K\alpha$ line, and the $K\alpha$ line of nickel. The lines are included at the appropriate normalization for the assumed inclination, abundance, and reflection fraction. Hence, **pexmon** is superior to the usual “**pexrav**+**gaussian**” model since the strengths of the Compton reflection continuum and fluorescent lines are forced to be self-consistent. Assumptions do need to be made, however, when employing this model. In particular, we fix the inclination parameter of this component to be $i = 60^\circ$ and assume cosmic abundances.

3.2. Guidance from the long *Chandra*/HETG observation

It is well known that NGC 3783 possesses a high-column density warm absorber (WA; e.g., Reynolds 1997); this is the greatest complexity we face when modeling the X-ray spectrum of this source. For guidance, we turn to the long (900 ks) observation of NGC 3783 with the HETGS on *Chandra*. Extensive analyses of the HETG data have been published (Kaspi et al. 2002; Krongold et al. 2003; Netzer et al. 2003); however, to retain consistency and utilize the latest calibrations, we have retrieved these data from the TGCAT database⁴ and have reanalyzed the 1st-order MEG+HEG spectra.

In more detail, we obtain the *Chandra*HETG-data for NGC 3783 from TGCAT for each of the OBSIDs corresponding to the 900 ks campaign and, coadd together spectra for a given order of a given grating. As a result, we obtain four spectral files corresponding to the time-average ± 1 st order spectrum from each of the HEG and the MEG. These were binned to a minimum of 15 photons per spectral bin in order to validate the use of χ^2 techniques while still maintaining spectral resolution. We then jointly analyzed these spectra, noticing the 0.5–7 keV range in the MEG data and the 1–7.5 keV range in the HEG data. We permitted the overall cross-normalization between these four spectra to be free parameters; in all cases, the best-fitting cross-normalization is within 5% of unity.

Fitting these data with a power-law modified by the effects of Galactic absorption ($N_H = 9.91 \times 10^{20} \text{ cm}^{-2}$; described using the **phabs** model of XSPEC) results in a very poor fit with $\chi^2/\nu = 58962/13112$ (4.50). The residuals suggest a soft excess component, soft X-ray absorption by a WA, and a prominent fluorescent iron $K\alpha$ line at 6.4 keV. The effect of the WA is modeled using the XSTAR code (Kallman & Bautista 2001); for an absorber of a given column density N_H and ionization parameter ξ , XSTAR is used to compute the absorption imprinted on a power-law X-ray spectrum. We compute a grid of XSTAR models, logarithmically sampling a range of column densities in the range $N_H : 10^{20} - 10^{24} \text{ cm}^{-2}$ and a range of ionization parameters in the range $\xi : 1 - 10^4 \text{ erg cm s}^{-1}$, for use in spectral fitting. In the construction of the WA grids it is assumed that elemental abundances are fixed to solar values⁵, and that the turbulent velocity of the WA is 200 km s^{-1} . Dramatic improvements in the goodness-of-fit are found by the inclusion in the model of three zones of WA. To begin with, each WA component is included assuming that the absorbing gas is at rest with respect to NGC 3783; the improvement in the fit upon the addition of each WA component was $\Delta\chi^2 = -26316, -3096$ and -2490 . The inclusion of a fourth zone led to a

⁴<http://tgcath.mit.edu/>

⁵<http://heasarc.nasa.gov/lheasoft/xstar/docs/html/node41.html>

much smaller improvement in the fit and hence was deemed inappropriate. The residuals from the 3-WA fit do indicate a soft excess. Following Krongold et al. (2003), we model the soft excess with a blackbody component (this is intended to be a phenomenological, not a physical, description of the soft excess; see discussion in §3.3) resulting in an improvement in the fit of $\Delta\chi^2/\Delta\nu = -480/-2$ (i.e., $\chi^2/\nu = 26582/13104$ (2.03)).

While providing a decent fit to the global spectrum, the model thus described leaves prominent unmodeled emission and absorption lines, the most prominent of which is the iron fluorescent emission line at 6.4 keV. Fitting the iron line with a simple Gaussian model improves the goodness-of-fit by $\Delta\chi^2/\Delta\nu = -593/-3$, with a line energy $E = 6.398 \pm 0.002$ keV (confirming the identification of cold iron- $K\alpha$), FWHM = 2000 ± 300 km s⁻¹ and equivalent width $W_{K\alpha} = 88 \pm 6$ eV. However, since we believe that this component originates from reflection, we shall henceforth model it using **pexmon**; replacing the simple Gaussian with the **pexmon** model convolved with a Gaussian velocity profile (with FWHM = 1800 ± 300 km s⁻¹) results in a slightly better fit ($\Delta\chi^2 = -18$). At the soft end of the spectrum, the $K\alpha$ emission triplet of O VII (at 0.574 keV, 0.569 keV, 0.561 keV) as well as the $K\alpha$ emission line of O VIII (at 0.654 keV) are clearly visible. Modeling these as Gaussian lines at the redshift of NGC 3783 with common velocity width yields a further improvement in the goodness of fit ($\Delta\chi^2 = -218$) with best-fitting FWHM = 700 ± 150 km s⁻¹ and equivalent widths $W_{0.574} = 26 \pm 6$ eV, $W_{0.569} = 14 \pm 6$ eV, $W_{0.561} = 47 \pm 9$ eV, and $W_{0.654} = 23 \pm 5$ eV.

It is well known that the WA in this and many other objects corresponds to outflowing gas. Relaxing the constraint that the WA zones are at the systemic redshift of NGC 3783 yields a large improvement in the fit ($\Delta\chi^2/\Delta\nu = 4247/-3$; $\chi^2/\nu = 21532/13094$ (1.64)), with implied line-of-sight outflow velocities in the 500 – 1000 km s⁻¹ range. These velocities as well as the other parameters defining the best-fit model for the HETG data are listed in Table 1. The spectral model described in this section (power-law continuum, three-zone WA, blackbody soft excess, reflection from distant neutral material, and emission lines from O VII and O VIII) describes the vast majority of spectral features seen in the HETG data (see Fig. 3).

3.3. Global Modeling of the 0.7–45 keV Spectrum

To extract the maximal information from the full-band (0.7–45 keV) *Suzaku* spectrum of NGC 3783, we must compare the data to a global spectral model which is as physically self-consistent and realistic as possible. In constructing this global model, we draw guidance from our heuristic analysis of the hard-band spectrum (§3.1) as well as the results from the *Chandra*/HETG (§3.2). The primary continuum emission is taken to be a power-law

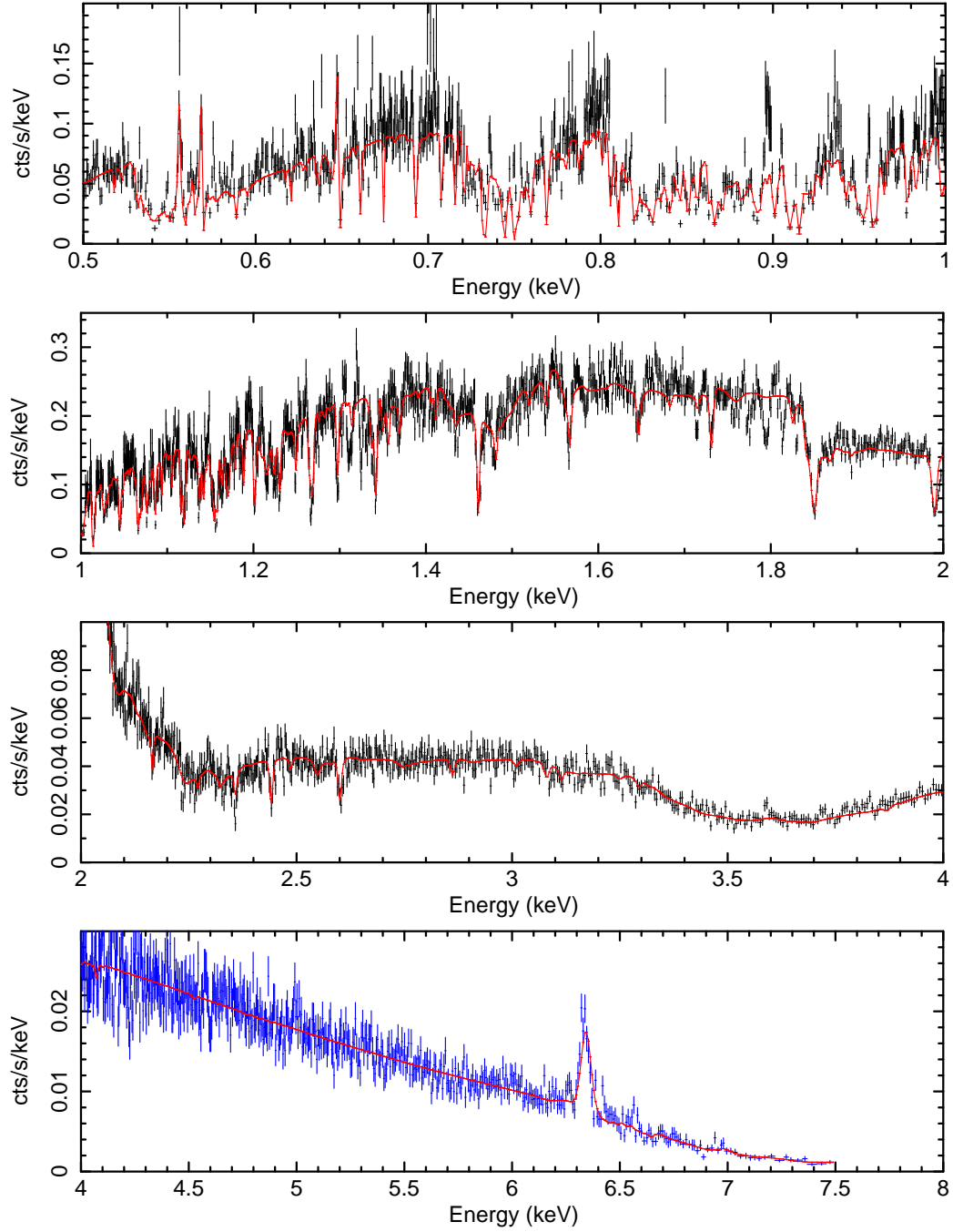


Fig. 3.— Folded *Chandra*/HETG spectrum and best fitting model as a function of observed energy. As described in the text (§3.2), the model is fitted simultaneously to the ± 1 MEG (0.5–7 keV) and HEG (1–7.5 keV) data. However, for clarity, we only show here the -1 -order MEG data (black; first three panels) and the -1 -order HEG data (blue; bottom panel).

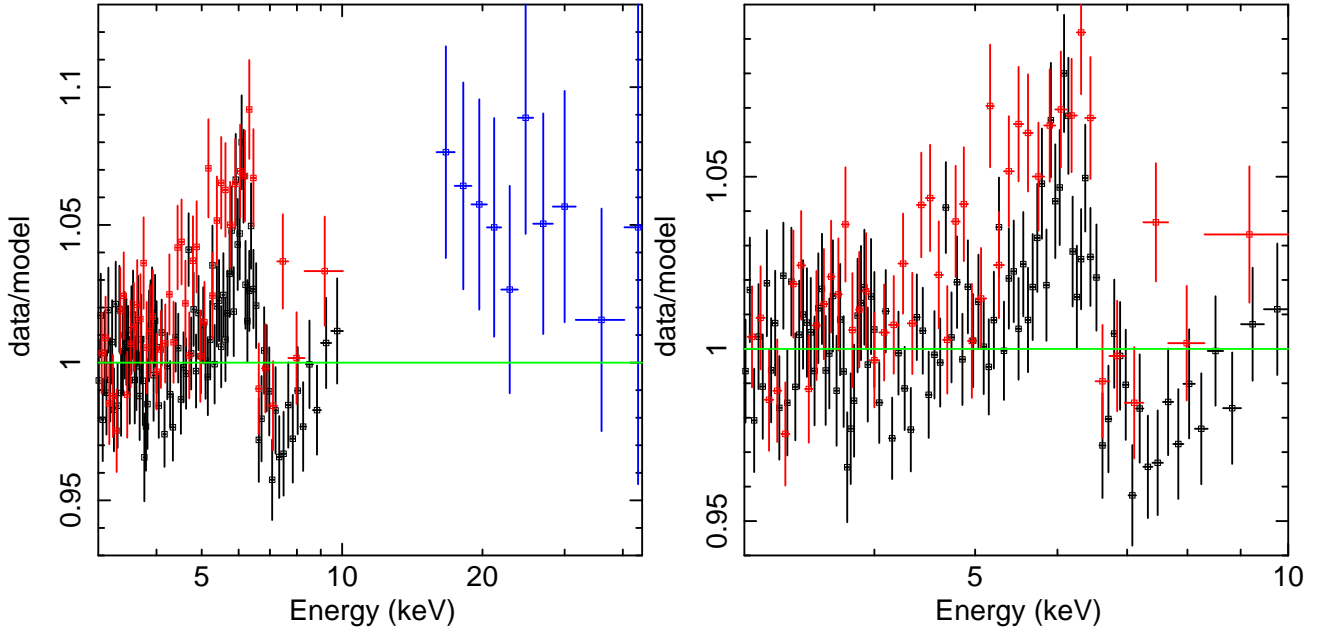


Fig. 4.— Results of fitting the XIS+PIN spectrum with a model that includes the warm absorbers, distant reflection and scattering/leaked soft component but not the relativistic ionized accretion disk. While the fitting is performed on the 0.7–45 keV spectrum, we show for clarity only the residuals above 3 keV. *Left:* Strong residuals indicative of a broad iron line and Compton reflection hump are clearly visible. This motivates the inclusion of a relativistic disk component into the spectral model. The XIS 0+3 data are shown in black and XIS 1 data are in red, while the HXD/PIN data are in blue. The solid green line represents a data-to-model ratio of unity. *Right:* Zoom-in on the Fe K line region.

(photon index Γ) with a soft excess which we describe as a blackbody (temperature T). X-ray reflection of this continuum from cold, distant material (possibly associated with the dusty/molecular torus of unified Seyfert schemes) is described using the `pexmon` model (see §3.1). As discussed in §3.1, the inclination of the `pexmon` is fixed at $i = 60^\circ$ and the abundances are fixed to be solar, as defined in Nandra et al. (2007). These emission components are then absorbed by a three-zone WA modeled using the XSTAR tables described in §3.2; the column density N_W and ionization parameter ξ of each zone is taken to be a free parameter rather than being fixed to the HETG value. Since the *Suzaku*/XIS detectors do not have the spectral resolution capable of constraining the outflow velocities of the various WA zones, we have elected to hold the redshifts of these components fixed at the cosmological value for NGC 3783. Statistically indistinguishable results are obtained if we, instead, fix the outflow velocities to the HETG-derived values. For completeness, we also allow for some fraction f_{sc} of the continuum to be scattered around (or leak through) the WAs, i.e., our

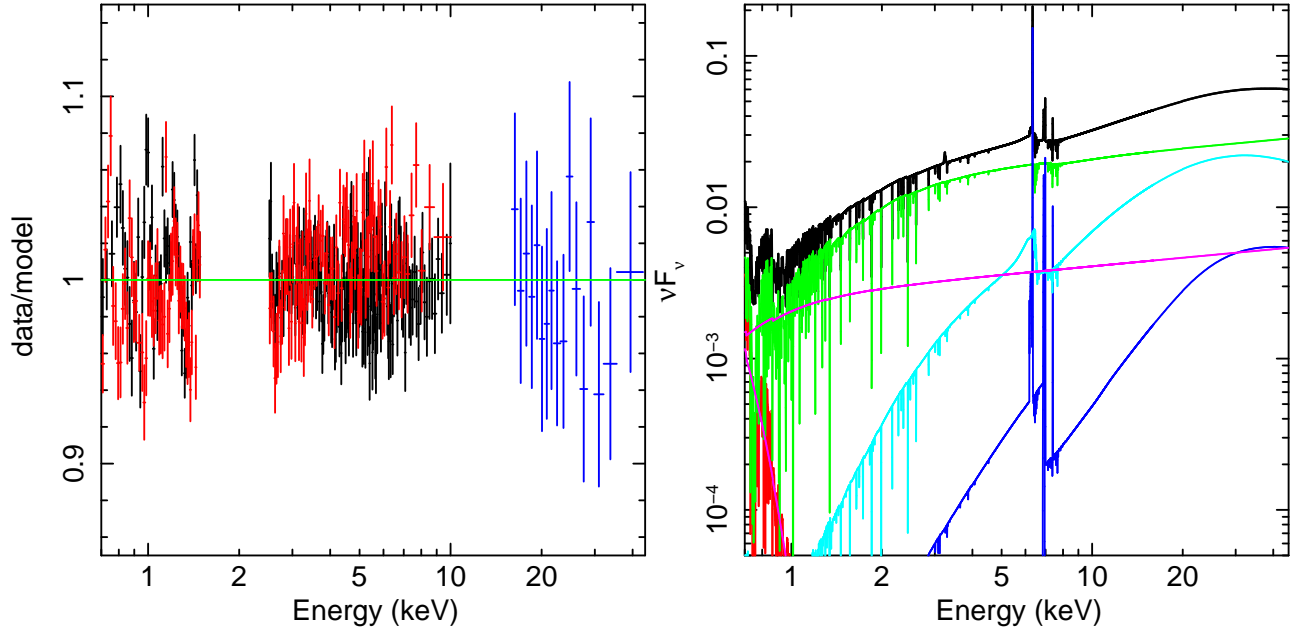


Fig. 5.— Global modeling of the 0.7 – 45 keV XIS-FI+PIN data. The *left panel* shows the resulting residuals from fitting the model (including the relativistic accretion disk) discussed in §3.3. Data point colors are as in Fig. 2. The *right panel* shows the best-fitting model color coded as follows: (a) green line, continuum power-law emission; (b) dark blue line, cold and ionized iron line emission from distant matter; (c) red line, soft excess modeled as blackbody; (d) magenta line, significant emission that scatters around or leaks through the warm absorber; (e) light blue line, relativistically-smearred disk reflection, (f) thick black line, total summed model spectrum. Warm absorption affects all components apart from (d).

model allows for “partial covering”.

Fitting this model to the 0.7–45 keV *Suzaku* data results in a poor fit ($\chi^2/\nu = 1206/679$ (1.78)) and strong residuals which indicate the presence of the broad iron line as well as additional reflection beyond that associated with the narrow iron line (Fig. 4). This leads us to include relativistically smeared reflection from an ionized accretion disk into the spectral model; operationally, we use the ionized reflection model `relionx` (Ross & Fabian 2005) convolved with the variable spin relativistic smearing model `relconv` (Dauser et al. 2010). The `relconv` model is a further evolution of the `kerrconv` model of Brenneman & Reynolds (2006), employing faster and more accurate line-integration schemes and allowing black hole spin to be fit as a free parameter for prograde, non-spinning and retrograde spins ($a \in [-0.998, 0.998]$). While the fit achieved with this blurred reflection model is not statistically ideal ($\chi^2/\nu = 917/664$ (1.38)), there are no broad-band residuals (Fig. 5a), and much of the contribution to the excess χ^2 originates from fine details of the WA-dominated

region below 1.5 keV. The model is shown in Fig. 5b, and the best-fitting parameter values are shown in Table 1.

The parameters defining the best-fitting model for the 0.7 – 45 keV data are shown in Table 1 along with their 90% confidence ranges. Under the assumption that we can identify the low-, medium-, and high-ionization components seen in the 2001-HETG observation with those seen in our 2009-*Suzaku* data, we see that both the column density and the ionization state of the low-ionization absorber have increased somewhat ($\Delta \log \xi \approx 0.28$, $\Delta N_{\text{WA}} \approx 3 \times 10^{21} \text{ cm}^{-2}$). In contrast, the medium- and high-ionization absorbers have slightly dropped in ionization parameter. Given that these different zones are likely at very different distances from the central engine with very different plasma densities, they will possess very different recombination/photoionization timescales and hence will respond to changes in the ionization flux on different timescales. Thus, it is not surprising that we see a mixture of increasing and decreasing ionization states in the various WA zones.

We also note a change in both the temperature and normalization of the blackbody component between the 2001-HETG and 2009-*Suzaku* data. This merits some discussion. The blackbody component used to phenomenologically parameterize the soft excess was first employed by Krongold et al. (2003), who found $kT = 0.10 \pm 0.03 \text{ keV}$ and $A_{\text{bb}} = 2.0 \pm 0.7 \times 10^{-4}$, where the normalization is in units of L_{39}/D_{10}^2 (L_{39} is luminosity of the component in units of $10^{39} \text{ erg s}^{-1}$ and D_{10} is distance to the source in units of 10 kpc). Our analysis of the same HETG data confirms the Krongold et al. (2003) result. By contrast, our analysis of the *Suzaku*/XIS+PIN spectra finds a lower temperature ($kT = 0.060_{-4}^{+3} \text{ keV}$) and a normalization that is almost two orders of magnitude greater ($A_{\text{bb}} = 8.4_{-2.7}^{+6.0} \times 10^{-3}$). We stress that neither the use of a blackbody to model the soft excess nor the precise change in the parameters of the blackbody should be interpreted literally. In particular, the significant change in the normalization of this component is misleading — the lower energy cutoffs in both the HETG analysis (0.5 keV) and the XIS analysis (0.7 keV) are much higher than the peak of this blackbody component and, thus, only the Wien tail of this component is playing any role in the spectral fitting. Given this fact, even a modest drop in the temperature must be compensated for by a large increase in normalization in order to have a comparable contribution in the observed energy band. While the physical nature of the soft excess is of intrinsic interest, it is beyond the scope of this paper. We have verified that different treatments of the soft excess (replacing the blackbody spectrum with bremsstrahlung or a steep power-law component) do not affect the interpretation of the spectrum above 2 keV.

The principal focus of this work is the signature of the relativistic accretion disk. Our global fit finds reflection from a rather low-ionization accretion disk ($\xi < 9 \text{ erg cm s}^{-1}$) extending down to the innermost stable circular orbit (ISCO) of a rapidly rotating black hole

($a \geq 0.98$). The emissivity/irradiation profile defining the reflection spectrum, modeled as a broken power-law, is found to have an inner power-law index of $q_1 = 5.2^{+0.7}_{-0.8}$ breaking to $q_2 = 2.9 \pm 0.2$ at a radius of $r_{\text{br}} = 5.4^{+1.9}_{-0.9} r_g$. If these indices are tied together in the model, i.e., if $q_1 = q_2$, the fit worsens considerably ($\Delta\chi^2/\Delta\nu = +21/+1$, with $q_1 = q_2 = 3.0 \pm 0.3$) and the black hole spin is also less tightly constrained: $a \geq 0.25$.

The iron abundance of the disk has been constrained to lie between 2.8 – 4.6 times solar. To probe the robustness of this constraint we have refitted the data in three different ways, each allowing for slight differences in the way the iron abundance was handled in our model: (1) fixing Fe/solar of the distant reflector (**pexmon**) to that of the inner disk reflection (**reflionx**), with both values frozen at Fe/solar = 1; (2) allowing these linked abundances allowed to vary freely; and (3) allowing both abundances to vary freely and independently. Compared with the global best-fit, scenario (1) resulted in a worsening of goodness-of-fit by $\Delta\chi^2 = 33$ and unconstrained black hole spin at the 90% confidence level, scenario (2) resulted in a marginal decrease in goodness-of-fit by $\Delta\chi^2 = 7$ (no change in spin constraints) and scenario (3) yielded no change in the goodness-of-fit (no change in spin constraints). In summary, the high iron abundance of the **reflionx** is statistically preferred to the solar value; the high spin value is dependent upon the high iron abundance, but the high abundance is strongly preferred in the fit. Because the iron abundance of the distant reflector could not be constrained independently of the relativistic reflector, the **pexmon** and **reflionx** iron abundances have been linked in our best model fit.

To gauge the importance of the (complex) soft spectrum on our global fit, we have also conducted a restricted hard-band (3–45 keV) fit. Since a hard-band fit cannot constrain the parameters of the WA or soft excess, these parameters are constrained to lie within their 90% confidence ranges as derived from the 0.7–45 keV analysis. To be most conservative, we also relax the constraint on the XIS/PIN cross-normalization, allowing it to be a free parameter. The resulting fit is listed in the last column of Table 1. For this fit $\chi^2/\nu = 499/527$ (0.95), a great improvement over the 0.7 – 45 keV fit, and confirmation that the small residuals below ~ 1.5 keV are the primary contribution to the large reduced χ^2 of the full spectral fit. While the parameter values are equivalent to those of the 0.7 – 45 keV fit within errors, the uncertainties on the parameters are larger when only the hard spectrum is considered. This is especially true for the inner disk emissivity and break radius of the **relconv** model, which exhibit a strong degeneracy without the soft spectrum data. Figure 6 shows the confidence contours on the (q_1, q_2) -plane for this hard band fit; we see that the outer disk emissivity index, q_2 , is well-constrained, whereas the constraints on the inner disk emissivity index, q_1 , are clearly worse. Fixing the XIS/PIN cross-normalization at the nominal value of 1.18 tightens the constraints but still leaves a significant degeneracy between q_1 and r_{br} . (Fig. 6).

Using the best-fitting $0.7 - 45$ keV spectral model with the XIS 0 normalization, the $2 - 10$ keV observed-frame flux of NGC 3783 is $F_{2-10} = 6.04 \times 10^{-11} \text{ erg cm}^{-2} \text{ s}^{-1}$. Adopting a standard cosmological model ($H_0 = 71 \text{ km s}^{-1} \text{ Mpc}^{-1}$, $\Omega_M = 0.3$, $\Omega_\Lambda = 0.7$), this implies a rest-frame luminosity of $L_{2-10} = 1.26 \times 10^{43} \text{ erg s}^{-1}$. The hard X-ray band yields a $16 - 45$ keV flux of $F_{16-45} = 1.07 \times 10^{-10} \text{ erg cm}^{-2} \text{ s}^{-1}$ for a rest-frame luminosity of $L_{16-45} = 2.24 \times 10^{43} \text{ erg s}^{-1}$.

3.4. The Spin of the Black Hole

Our fiducial spectral model discussed above yields a spin constraint of $a \geq 0.98$ (90% confidence), or $a \geq 0.88$ (99% confidence). However, given the subtle nature of the spin measurements, it is useful to address the systematic issues that may be introduced by the modeling and analysis techniques.

We can assess the role of different analysis-related assumptions on the derived spin by comparing the variation of χ^2 with a . Figure 7 (black line) shows $\Delta\chi^2(a) = \chi^2(a) - \chi^2_{\text{best-fit}}$ from our fiducial analysis that underlies the constraint just quoted. It is interesting to note the non-monotonic nature of the χ^2 -space above $a \sim 0.75$. We consider a few variants from this fiducial analysis in order to probe the sensitivity of the spin measurement. An important issue is the extent to which the warm absorber parameters are trading-off with the derived black hole spin. Thus, we repeat the analysis with the warm absorber parameters (column densities and ionization parameters for all three zones) fixed at their best-fit values from the fiducial model. The resulting spin constraints are shown in Fig. 7 ($a \geq 0.98$; red line) and are very similar to the fiducial model, indicating little or no degeneracy between spin and the warm absorber parameters.

Secondly, to the extent that the strength of the Compton reflection hump is important, we may be concerned about the effect of cross-calibration errors in the flux normalization between the XIS and the PIN spectra. Thus, we repeat the spectral analysis, leaving the cross-normalization factor as a free parameter. The best-fit value is slightly smaller than our fiducial value (1.15 vs. 1.18), but the improvement in the goodness-of-fit is only marginally significant ($\Delta\chi^2 = 6$ for one additional degree of freedom). The spin is constrained to be slightly smaller than that of the fiducial model (to 90% confidence, $a = 0.92 - 0.95$; Fig. 7, blue line).

Lastly, we may be concerned that the spin fits are being driven by the contribution of the ionized disk to the high-S/N by highly-complex region of the spectrum below 1.5 keV. Thus, we have repeated our analysis including data only above 3 keV. Here, too, we allow

Model component	Parameter	HETG	Suzaku (0.7 – 45 keV)	Suzaku (> 3 keV)
Galactic column	N_{H}	9.91(<i>f</i>)	9.91(<i>f</i>)	9.91(<i>f</i>)
WAbs1	N_{WA}	$51.7^{+0.8}_{-0.7}$	90^{+10}_{-14}	90(<i>f</i>)
	$\log \xi$	$1.15^{+0.01}_{-0.01}$	$1.47^{+0.03}_{-0.03}$	1.47(<i>f</i>)
	Δz	$-(1.4^{+0.07}_{-0.07}) \times 10^{-3}$	0(<i>f</i>)	0(<i>f</i>)
WAbs2	N_{WA}	$127^{+1.8}_{-2.0}$	159^{+31}_{-21}	159(<i>f</i>)
	$\log \xi$	$2.08^{+0.01}_{-0.01}$	$1.93^{+0.02}_{-0.01}$	1.93(<i>f</i>)
	Δz	$-(1.0^{+0.3}_{-0.3}) \times 10^{-3}$	0(<i>f</i>)	0(<i>f</i>)
WAbs3	N_{WA}	268^{+10}_{-12}	168^{+48}_{-42}	168(<i>f</i>)
	$\log \xi$	$2.83^{+0.01}_{-0.01}$	$2.53^{+0.05}_{-0.02}$	2.53(<i>f</i>)
	Δz	$-(3.4^{+0.4}_{-0.4}) \times 10^{-4}$	0(<i>f</i>)	0(<i>f</i>)
PL	Γ	$1.62^{+0.01}_{-0.01}$	$1.81^{+0.10}_{-0.05}$	$1.84^{+0.06}_{-0.05}$
	A_{pl}	$(1.49^{+0.01}_{-0.01}) \times 10^{-2}$	$(1.46^{+0.09}_{-0.04}) \times 10^{-2}$	$(1.52^{+0.10}_{-0.08}) \times 10^{-2}$
BB	$kT(\text{eV})$	107^{+3}_{-3}	60^{+3}_{-4}	60(<i>f</i>)
	A_{bb}	$(1.4^{+0.1}_{-0.1}) \times 10^{-4}$	$(8.45^{+5.98}_{-2.67}) \times 10^{-3}$	$8.45 \times 10^{-3}(\text{f})$
Scattered fraction	f_{sc}	$(2.3^{+0.4}_{-1.0}) \times 10^{-2}$	$0.17^{+0.02}_{-0.02}$	0.17(<i>f</i>)
Cold Reflection	$\mathcal{R}_{\text{cold}}$	$0.49^{+0.04}_{-0.03}$	$0.46^{+0.12}_{-0.07}$	$0.62^{+0.31}_{-0.20}$
	PL cutoff (keV)	–	200(<i>f</i>)	200(<i>f</i>)
GAU line	E (keV)	–	6.97(<i>f</i>)	6.97(<i>f</i>)
	σ (keV)	–	0.0154(<i>f</i>)	0.0154(<i>f</i>)
	W_{FeXXVI} (eV)	–	22^{+5}_{-5}	18^{+6}_{-5}
	A_{FeXXVI}	–	$(1.28^{+0.29}_{-0.31}) \times 10^{-5}$	$(1.11^{+0.39}_{-0.31}) \times 10^{-5}$
Accretion disk	Z_{Fe}	–	$3.7^{+0.9}_{-0.9}$	$2.2^{+2.4}_{-0.9}$
	ξ	–	< 8	< 67
	\mathcal{R}_{rel}	–	$0.21^{+1.56}_{-0.07}$	$0.23^{+14.66}_{-0.03}$
	i	–	22^{+3}_{-8}	19^{+6}_{-14}
	r_{in}	–	ISCO(<i>f</i>)	ISCO(<i>f</i>)
	q_1	–	$5.2^{+0.7}_{-0.8}$	$4.7^{+1.9}_{-1.2}$
	r_{br}	–	$5.4^{+1.9}_{-0.9}$	$6.0^{+16.9}_{-1.9}$
	q_2	–	$2.9^{+0.2}_{-0.2}$	$2.8^{+0.3}_{-0.5}$
	r_{out}	–	400(<i>f</i>)	400(<i>f</i>)
PIN/XIS norm		–	1.18(<i>f</i>)	$1.15^{+0.07}_{-0.07}$
SMBH spin	a	–	≥ 0.98	$0.98^{+0.02}_{-0.34}$
χ^2/ν		21532/13094 (1.64)	917/664 (1.38)	499/527 (0.95)

Table 1: Spectral fit parameters. All errors are quoted at the 90% confidence level for one interesting parameter ($\Delta\chi^2 = 2.7$). Parameters marked with an “(f)” had their values fixed during the fit. Units of normalization are in $\text{ph cm}^{-2} \text{s}^{-1}$, column density is in units of 10^{20}cm^{-2} , ionization parameter is in erg cm s^{-1} , iron abundance is relative to solar (linked between the **reflionx** and **pexmon** reflection components), inclination is in degrees, radii are in r_g , and spin parameter is dimensionless, but is defined as $a \equiv cJ/GM^2$. See §3 for details.

the XIS/PIN cross-normalization to be a free parameter. Given the lack of data at soft energies to constrain them, the WA, BB and scattered fraction components were frozen to their best-fitting values for the full-band, free cross-normalization case (which is, within errors, identical to the WA parameters for the fiducial model). Yet again, the best-fit spin parameter is similar to that of the fiducial model ($a \geq 0.95$; Fig. 7, green line). This indicates that the fitted spin value is indeed driven by the Fe K band.

4. Discussion and Conclusions

The X-ray spectrum of NGC 3783 is complicated; in addition to the effects of a multi-zone warm absorber, there are suggestions that some fraction (17%) of the primary X-ray emission can scatter around or leak through the warm absorber. However, despite this complexity, the high-S/N and broad bandpass of *Suzaku* allows us to robustly detect and study the relativistically-smeared X-ray reflection spectrum from the surface of the inner accretion disk. Assuming that the region within the general relativistic radius of marginal stability does not contribute to the reflection spectrum (Reynolds & Fabian 2008) we determine a lower limit of $a \geq 0.98$ (90% confidence) to the dimensionless spin parameter of the black hole. Even at the 99% confidence level, we can constrain the spin to be $a \geq 0.88$. Relaxing the assumed XIS/PIN cross-normalization or neglecting the soft-band data (but then freezing the WA parameters) allows the model to find a slightly better fit and makes the constraints slightly lower ($a = 0.92 - 0.95$, $a \geq 0.95$ at 90% confidence, respectively; $a \geq 0.88$, $a \geq 0.90$ at 99% confidence, respectively).

Including this result, four out of eight of the AGN with reliable spin measurements may have spins greater than $a = 0.8$ (see Table 2). Spin measurements for more sources are required before we can draw any conclusions about the spin distribution function, but here we note that there are potentially important selection effects biasing any flux-limited sample towards high spin values. For standard accretion models, the efficiency of black hole accretion increases as the spin of the black hole increases. So, all else being equal, an accreting, rapidly spinning black hole will be more luminous than an accreting, slowly spinning black hole and hence will be over-represented in flux-limited samples.

We illustrate this effect by calculating the selection bias given some very simple assumptions. Suppose that a flux limited sample is constructed in some band B. The accretion luminosity in that band will be given by

$$L = K_B \eta \dot{M} c^2, \quad (1)$$

where K_B is the fraction of luminosity appearing in band B (i.e. the reciprocal of the

AGN	a	$W_{K\alpha}$	q_1	Fe/solar	ξ	log M	$L_{\text{bol}}/L_{\text{Edd}}$	Host	WA
MCG–6-30-15 ^a	≥ 0.98	305^{+20}_{-20}	$4.4^{+0.5}_{-0.8}$	$1.9^{+1.4}_{-0.5}$	68^{+31}_{-31}	$6.65^{+0.17}_{-0.17}$	$0.40^{+0.13}_{-0.13}$	E/S0	yes
Fairall 9 ^b	$0.65^{+0.05}_{-0.05}$	130^{+10}_{-10}	$5.0^{+0.0}_{-0.1}$	$0.8^{+0.2}_{-0.1}$	$3.7^{+0.1}_{-0.1}$	$8.41^{+0.11}_{-0.11}$	$0.05^{+0.01}_{-0.01}$	Sc	no
SWIFT J2127.4+5654 ^c	$0.6^{+0.2}_{-0.2}$	220^{+50}_{-50}	$5.3^{+1.7}_{-1.4}$	$1.5^{+0.3}_{-0.3}$	40^{+70}_{-35}	$7.18^{+0.07}_{-0.07}$	$0.18^{+0.03}_{-0.03}$	—	yes
1H0707–495 ^d	≥ 0.98	1775^{+511}_{-594}	$6.6^{+1.9}_{-1.9}$	≥ 7	50^{+40}_{-40}	$6.70^{+0.40}_{-0.40}$	$\sim 1.0_{-0.6}$	—	no
Mrk 79 ^e	$0.7^{+0.1}_{-0.1}$	377^{+47}_{-34}	$3.3^{+0.2}_{-0.1}$	1.2*	177^{+6}_{-6}	$7.72^{+0.14}_{-0.14}$	$0.05^{+0.01}_{-0.01}$	SBb	yes
Mrk 335 ^f	$0.70^{+0.12}_{-0.01}$	146^{+39}_{-39}	$6.6^{+2.0}_{-1.0}$	$1.0^{+0.1}_{-0.1}$	207^{+5}_{-5}	$7.15^{+0.13}_{-0.13}$	$0.25^{+0.07}_{-0.07}$	S0a	no
NGC 7469 ^f	$0.69^{+0.09}_{-0.09}$	91^{+9}_{-8}	≥ 3.0	≤ 0.4	≤ 24	$7.09^{+0.06}_{-0.06}$	$1.12^{+0.13}_{-0.13}$	SAB(rs)a	no
NGC 3783 ^g	≥ 0.98	263^{+23}_{-23}	$5.2^{+0.7}_{-0.8}$	$3.7^{+0.9}_{-0.9}$	≤ 8	$7.47^{+0.08}_{-0.08}$	$0.06^{+0.01}_{-0.01}$	SB(r)ab	yes

Table 2: Summary of black hole spin measurements derived from relativistic reflection fitting of SMBH spectra. Data are taken with *Suzaku* except for 1H0707–495, which was observed with *XMM-Newton*, and MCG–6-30-15, in which the data from *XMM* and *Suzaku* are consistent with each other. Spin (a) is dimensionless, as defined previously. $W_{K\alpha}$ denotes the equivalent width of the broad iron line relative to the continuum in units of eV. Parameter q_1 represents the inner disk emissivity index and is unitless. Fe/solar is the iron abundance of the inner disk in solar units, while ξ is its ionization parameter in units of erg cm s^{-1} . M is the mass of the black hole in solar masses, and $L_{\text{bol}}/L_{\text{Edd}}$ is the Eddington ratio of its luminous output. Host denotes the galaxy host type and WA denotes the presence/absence of a warm absorber. Values marked with an asterisk either were fixed in the fit or have unknown errors. All masses are from Peterson et al. (2004) except MCG–6-30-15, 1H0707–495 and SWIFT J2127.4+5654, which are taken from McHardy et al. (2005), Zoghbi et al. (2010) and Malizia et al. (2008), respectively. All bolometric luminosities are from Woo & Urry (2002) except for the same three sources. The same references for MCG–6-30-15 and SWIFT J2127.4+5654 are used, but host types for 1H0707–495 and SWIFT J2127.4+5654 are unknown.

^aBrenneman & Reynolds (2006), Miniutti et al. (2007).

^bSchmoll et al. (2009), though note some discrepancies with Patrick et al. (2010).

^cMiniutti et al. (2009), though note some discrepancies with Patrick et al. (2010).

^dZoghbi et al. (2010), de La Calle Pérez et al. (2010).

^eGallo et al. (2005, 2010).

^fPatrick et al. (2010).

^gThis work.

bolometric correction), η is the accretion efficiency, and \dot{M} is the mass accretion rate. Now let us assume that \dot{M} has no explicit spin dependence (e.g. is determined by the larger circumnuclear environment), and that the spectral energy distribution and hence K_B is independent of spin. Thus, the space density of sources with accretion rates in the range $\dot{M} \rightarrow \dot{M} + d\dot{M}$ and spins in the range $a \rightarrow a + da$, denoted $\Phi(\dot{M}, a) d\dot{M} da$, can be taken as a given function set by the astrophysics of black hole growth.

We assume a Euclidean universe, valid for the local/bright AGN samples relevant for spin measurements with the current generation of X-ray observatories. The number of sources in a flux-limited sample with luminosity in the range $L \rightarrow L + dL$ and spins in the range $a \rightarrow a + da$ is then,

$$dN \propto \Phi(L, a) L^{3/2} dL da, \quad (2)$$

where $\Phi(L, a) dL da$ is the space density of sources with luminosity in the range $L \rightarrow L + dL$ and spins in the range $a \rightarrow a + da$. Transforming into the (\dot{M}, a) -plane gives,

$$dN \propto \Phi(\dot{M}, a) \eta^{3/2} d\dot{M} da. \quad (3)$$

Using our assumption that the mass accretion rate is independent of spin, we can separate $\Phi(\dot{M}, a)$ into an accretion rate dependent space density $n(\dot{M})$ and a spin distribution function $f(a)$, $\Phi(\dot{M}, a) = n(\dot{M})f(a)$. We can then integrate Eqn. 3 over \dot{M} in order to determine the number of sources in a flux-limited sample with spins in the range $a \rightarrow a + da$:

$$dN_a \propto f(a) \eta(a)^{3/2} da \left(\int n(\dot{M}) d\dot{M} \right). \quad (4)$$

For illustration purposes, let us examine eqn. 4 in the case of a completely flat spin distribution where $f(a) = \text{constant}$ for $a \in [0, a_{\text{max}}]$ and is zero otherwise. Thus, half of the parent population as a whole has $a > a_{\text{max}}/2$. We find that if $a_{\text{max}} = 0.95$, then half of sources in the flux limited sample will have $a > 0.67$; for $a_{\text{max}} = 0.99$ we find that half of the sources in the sample have $a > 0.73$.

Generalizing away from a flat spin distribution, we can consider spin distribution functions of the form $f(a) \propto a^p$. Within this simple framework, we require $f(a) \propto a$ (i.e. $p = 1.0$) in order to produce flux-limited samples where half of sources have $a > 0.84$ (assuming $a_{\text{max}} = 0.95$). For high-spin weighted distribution functions such as this, the selection bias is stronger; only 20% of objects in the volume-limited parent sample actually have $a > 0.84$. Of course, given the small number statistics and highly inhomogeneous selection functions for the current spin measurements, it is too early to draw any conclusions about the need for a high-spin biased distribution function.

We are extremely grateful to our NASA and JAXA colleagues in the *Suzaku* project for enabling these Key Project data to be collected. We thank Martin Elvis and Cole Miller for

insightful conversations throughout the course of this work, and the anonymous referee, who provided useful feedback that has improved this manuscript. This work was supported by NASA under the *Suzaku* Guest Observer grant NNX09AV43G.

REFERENCES

- Arnaud, K. A. 1996, in *Astronomical Society of the Pacific Conference Series*, Vol. 101, *Astronomical Data Analysis Software and Systems V*, ed. G. H. Jacoby & J. Barnes, 17–+
- Berti, E. & Volonteri, M. 2008, *ApJ*, 684, 822
- Blandford, R. D. & Znajek, R. L. 1977, *MNRAS*, 179, 433
- Brenneman, L. W. & Reynolds, C. S. 2006, *ApJ*, 652, 1028
- Dauser, T., Wilms, J., Reynolds, C. S., & Brenneman, L. W. 2010, *MNRAS*, 1460
- Fabian, A. C., Nandra, K., Reynolds, C. S., Brandt, W. N., Otani, C., Tanaka, Y., Inoue, H., & Iwasawa, K. 1995, *MNRAS*, 277, L11
- Fabian, A. C., Rees, M. J., Stella, L., & White, N. E. 1989, *MNRAS*, 238, 729
- Gallo, L. C., Miniutti, G., Miller, J. M., Brenneman, L. W., Fabian, A. C., Guainazzi, M., & Reynolds, C. S. 2011, *MNRAS*, 411, 607
- Hughes, S. A. & Blandford, R. D. 2003, *ApJ*, 585, L101
- Kallman, T. & Bautista, M. 2001, *ApJS*, 133, 221
- Kaspi, S., Brandt, W. N., George, I. M., Netzer, H., Crenshaw, D. M., Gabel, J. R., Hamann, F. W., Kaiser, M. E., Koratkar, A., Kraemer, S. B., Kriss, G. A., Mathur, S., Mushotzky, R. F., Nandra, K., Peterson, B. M., Shields, J. C., Turner, T. J., & Zheng, W. 2002, *ApJ*, 574, 643
- King, A. R. & Pringle, J. E. 2007, *MNRAS*, 377, L25
- Krongold, Y., Nicastro, F., Brickhouse, N. S., Elvis, M., Liedahl, D. A., & Mathur, S. 2003, *ApJ*, 597, 832
- Laor, A. 1991, *ApJ*, 376, 90

- Magdziarz, P. & Zdziarski, A. A. 1995, *MNRAS*, 273, 837
- Malizia, A., Bassani, L., Bird, A. J., Landi, R., Masetti, N., de Rosa, A., Panessa, F., Molina, M., Dean, A. J., Perri, M., & Tueller, J. 2008, *MNRAS*, 389, 1360
- McHardy, I. M., Gunn, K. F., Uttley, P., & Goad, M. R. 2005, *MNRAS*, 359, 1469
- Miller, J. M. 2007, *ARA&A*, 45, 441
- Miller, J. M., Fabian, A. C., Wijnands, R., Remillard, R. A., Wojdowski, P., Schulz, N. S., Di Matteo, T., Marshall, H. L., Canizares, C. R., Pooley, D., & Lewin, W. H. G. 2002, *ApJ*, 578, 348
- Miniutti, G., Panessa, F., de Rosa, A., Fabian, A. C., Malizia, A., Molina, M., Miller, J. M., & Vaughan, S. 2009, *MNRAS*, 398, 255
- Moderski, R. & Sikora, M. 1996, *MNRAS*, 283, 854
- Nandra, K., O’Neill, P. M., George, I. M., & Reeves, J. N. 2007, *MNRAS*, 382, 194
- Netzer, H., Kaspi, S., Behar, E., Brandt, W. N., Chelouche, D., George, I. M., Crenshaw, D. M., Gabel, J. R., Hamann, F. W., Kraemer, S. B., Kriss, G. A., Nandra, K., Peterson, B. M., Shields, J. C., & Turner, T. J. 2003, *ApJ*, 599, 933
- Patrick, A. R., Reeves, J. N., Porquet, D., Markowitz, A. G., Lobban, A. P., & Terashima, Y. 2010, *ArXiv e-prints*
- Penrose, R. 1969, *Nuovo Cimento Rivista Serie*, 1, 252
- Peterson, B. M., Ferrarese, L., Gilbert, K. M., Kaspi, S., Malkan, M. A., Maoz, D., Merritt, D., Netzer, H., Onken, C. A., Pogge, R. W., Vestergaard, M., & Wandel, A. 2004, *ApJ*, 613, 682
- Reis, R. C., Fabian, A. C., Ross, R. R., Miniutti, G., Miller, J. M., & Reynolds, C. 2008, *MNRAS*, 387, 1489
- Reynolds, C. S. 1997, *MNRAS*, 286, 513
- Reynolds, C. S. & Fabian, A. C. 2008, *ApJ*, 675, 1048
- Reynolds, C. S. & Nowak, M. A. 2003, *Phys. Rep.*, 377, 389
- Rezzolla, L., Barausse, E., Dorband, E. N., Pollney, D., Reisswig, C., Seiler, J., & Husa, S. 2008, *Phys. Rev. D*, 78, 044002

- Ross, R. R. & Fabian, A. C. 2005, MNRAS, 358, 211
- Schmoll, S., Miller, J. M., Volonteri, M., Cackett, E., Reynolds, C. S., Fabian, A. C., Brenneman, L. W., Miniutti, G., & Gallo, L. C. 2009, ApJ, 703, 2171
- Sikora, M., Stawarz, L., & Lasota, J. 2007, ApJ, 658, 815
- Tanaka, Y., Nandra, K., Fabian, A. C., Inoue, H., Otani, C., Dotani, T., Hayashida, K., Iwasawa, K., Kii, T., Kunieda, H., Makino, F., & Matsuoka, M. 1995, Nature, 375, 659
- Theureau, G., Bottinelli, L., Coudreau-Durand, N., Gouguenheim, L., Hallet, N., Loulergue, M., Paturel, G., & Teerikorpi, P. 1998, A&AS, 130, 333
- Volonteri, M., Madau, P., Quataert, E., & Rees, M. J. 2005, ApJ, 620, 69
- Wilson, A. S. & Colbert, E. J. M. 1995, ApJ, 438, 62
- Woo, J. & Urry, C. M. 2002, ApJ, 579, 530
- Yaqoob, T., Reeves, J. N., Markowitz, A., Serlemitsos, P. J., & Padmanabhan, U. 2005, ApJ, 627, 156
- Zoghbi, A., Fabian, A. C., Uttley, P., Miniutti, G., Gallo, L. C., Reynolds, C. S., Miller, J. M., & Ponti, G. 2010, MNRAS, 401, 2419

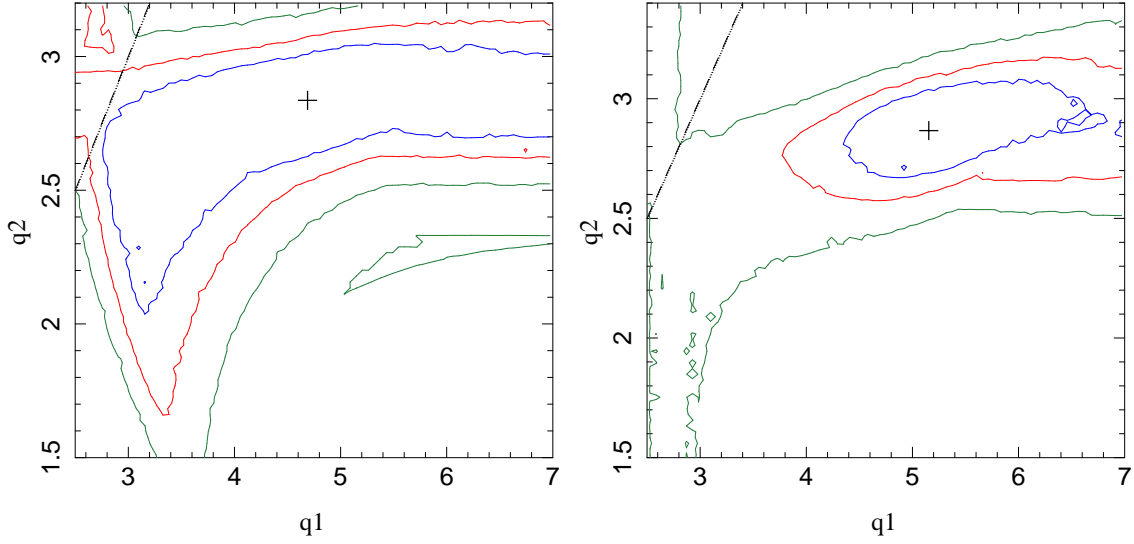


Fig. 6.— Confidence contours on the (q_1, q_2) -plane for the 3–45 keV band fit assuming a XIS/PIN cross-normalization that is free (left panel) or fixed at the nominal value of 1.18 (right panel). Blue, red and green lines show the 68%, 90% and 99% confidence contours for two interesting parameters ($\Delta\chi^2 = 2.3, 4.6, 9.2$), respectively. The dot-dashed black line represents $q_1 = q_2$.

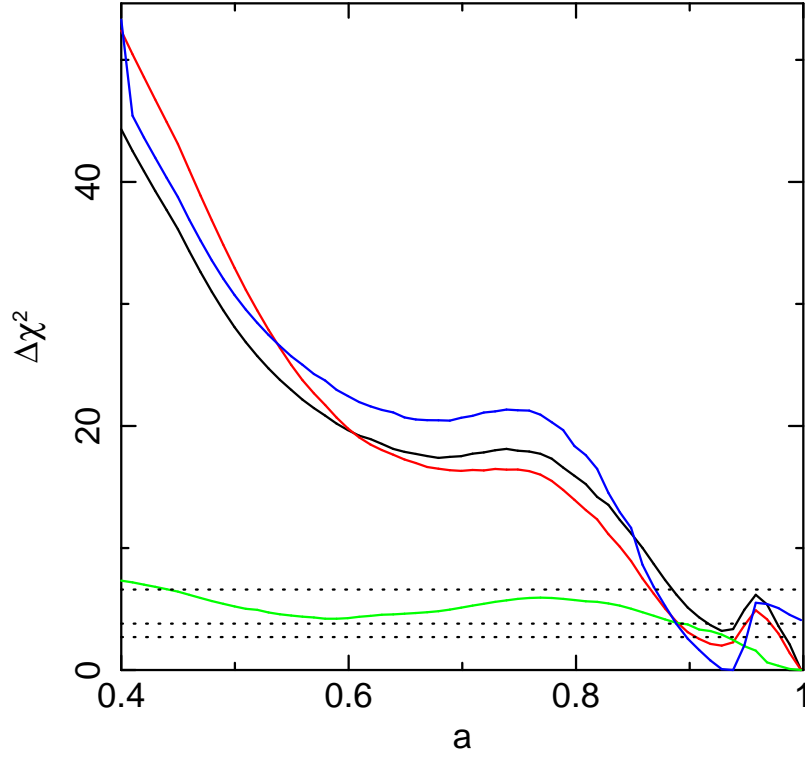


Fig. 7.— Goodness-of-fit parameter $\Delta\chi^2$ as a function of the assumed black hole spin for our fiducial model (black line), the fiducial model except with frozen WA parameters (red line), the fiducial model except with free XIS/PIN normalization (blue line), and a hard-band (> 3 keV) fit only (green line). Confidence levels are indicated with horizontal black lines and are derived for one interesting parameter. See text in §3.4 for details.